# Coarse-grained modeling of mitochondrial metabolism enables subcellular flux inference from fluorescence lifetime imaging microscopy

Xingbo Yang[1] and Daniel J. Needleman[1, 2]

[1]Department of Molecular and Cellular Biology and John A. Paulson School of Engineering and Applied Sciences, Harvard University, Cambridge, MA 02138. [2]Center for Computational Biology, Flatiron Institute, New York, United States

## Abstract

Mitochondria are central to metabolism and their dysfunctions are associated with many diseases[1-9]. Metabolic flux, the rate of turnover of molecules through a metabolic pathway, is one of the most important quantities in metabolism, but it remains a challenge to measure spatiotemporal variations in mitochondrial metabolic fluxes in living cells. Fluorescence lifetime imaging microscopy (FLIM) of NADH is a label-free technique that is widely used to characterize the metabolic state of mitochondria *in vivo*[10-18]. However, the utility of this technique has been limited by the inability to relate FLIM measurement to the underlying metabolic activities in mitochondria. Here we show that, if properly interpreted, FLIM of NADH can be used to quantitatively measure the flux through a major mitochondrial metabolic pathway, the electron transport chain (ETC), *in vivo* with subcellular resolution. This result is based on the use of a coarse-grained NADH redox model, which we test in mouse oocytes subject to a wide variety of perturbations by comparing predicted fluxes to direct biochemical measurements and by self-consistency criterion. Using this method, we discovered a subcellular spatial gradient of mitochondrial metabolic flux in mouse oocytes. We showed that this subcellular variation in mitochondrial flux correlates with a corresponding subcellular variation in mitochondrial membrane potential. The developed model, and the resulting procedure for analyzing FLIM of NADH, are valid under nearly all circumstances of biological interest. Thus, this approach is a general procedure to measure metabolic fluxes dynamically in living cells, with subcellular resolution.

## Introduction

Decades of extensive work have produced a remarkable body of detailed information about the biochemistry of mitochondrial energy metabolism[19]. In brief, pyruvate is transported into mitochondria, where it is broken down and its products enter the tricarboxylic acid cycle (TCA). The TCA is composed of a number of chemical reactions, which ultimately reduces $NAD^+$ to NADH. NADH and oxygen are then utilized by the electron transport chain (ETC) to pump hydrogen ions across the mitochondrial membrane. ATP synthase uses this proton gradient to power the synthesis of ATP from ADP[20]. One of the most fundamental aspects of mitochondrial energy metabolism are the fluxes through these pathways: i.e. the mitochondrial metabolic fluxes. However, despite the wealth of knowledge concerning mitochondrial biochemistry, it is still unclear what processes set mitochondrial metabolic fluxes in many contexts or precisely how these fluxes are misregulated in diseases. The limitations of current techniques for measuring mitochondrial metabolic fluxes presents a major challenge. In particular, there is a lack of

techniques to measure mitochondrial metabolic fluxes with subcellular spatial resolution. Bulk biochemical techniques, such as measures of oxygen consumption and nutrient uptake rates[21-23], and isotope tracing by mass spectrometry[24], require averaging over large populations of cells. Such techniques cannot resolve cellular, or subcellular, metabolic heterogeneity[25-26]. Biochemical approaches for measuring mitochondrial metabolic fluxes are also often destructive[24,27], and thus cannot be used to observe continual changes in fluxes over time. Fluorescence microscopy provides a powerful means to measure cellular and subcellular metabolic heterogeneity continuously and non-destructively, with high spatiotemporal resolution. However, while fluorescent probes can be used to measure mitochondrial membrane potential[28] and the concentration of key metabolites[29-32], it is not clear how to relate those observables to mitochondrial metabolic fluxes.

Endogenous NADH has long been used to non-invasively probe cellular metabolism because NADH is autofluorescent, while $NAD^+$ is not[14]. Fluorescence lifetime imaging microscopy (FLIM) of NADH autofluorescence allows quantitative measurements of the concentration of NADH, the fluorescence lifetimes of NADH, and the fraction of NADH molecules bound to enzymes[10-18]. It has been observed that the fraction of enzyme-bound NADH and NADH fluorescence lifetimes are correlated with the activity of oxidative phosphorylation, indicating that there is a connection between NADH enzyme-binding and mitochondrial metabolic fluxes[12-13]. The mechanistic basis of this empirical correlation has been unclear. Here we show, that if properly interpreted, FLIM of NADH can be used to quantitatively measure flux through the mitochondrial electron transport chain, and thus provides a means to measure mitochondrial metabolic fluxes. Our results are based on a general, coarse-grained NADH redox model that is valid under nearly all circumstances of biological interest. We validate this model in mouse oocytes subject to a range of perturbations by comparing predicted fluxes from FLIM to direct measurements of the rate of oxygen consumption, and by self-consistency criterion. Using this method, we discovered subcellular spatial gradients of mitochondrial metabolic fluxes in mouse oocytes. Thus, FLIM of NADH can be used to non-invasively and continuously measure mitochondrial metabolic fluxes with subcellular resolution.

We used meiosis II arrested mouse oocytes as a model system to study mitochondrial metabolism with FLIM of NADH. ATP synthesis in mouse oocytes occurs primarily through oxidative phosphorylation using pyruvate, without an appreciable contribution from glycolysis[22]. Mouse oocyte can be cultured *in vitro* using chemically well-defined media[33]. They can directly take up pyruvate supplied to them or derive it from lactate through the activity of lactate dehydrogenase (LDH)[34], and they can remain in a steady state for hours with unaltered metabolism. While NADH and NADPH are difficult to distinguish with fluorescence measurements, the concentration of NADH in mouse oocytes is 40 times greater than the concentration of NADPH[35], so the autofluorescence signal from these cells can be safely assumed to result from NADH.

## Results

### Quantifying mitochondrial metabolism as a function of oxygen level using FLIM of NADH

To investigate the impact of quantitatively perturbing mitochondria, we continually varied the concentration of oxygen in the media, from $50\pm2$ μM to $0.26\pm0.04$ μM, while imaging NADH autofluorescence of oocytes with FLIM (Fig. 1a, top, black curve). We used a machine-learning

based algorithm to segment mitochondria in the obtained images[36] (Fig. 1b and Fig.S1), allowing us to specifically study the response of NADH in mitochondria. The intensity of NADH in mitochondria, $I$, increased with decreasing oxygen concentration (Fig. 1a, top, red), as is readily seen from the raw images (Fig. 1a, middle). Restoring oxygen to its original level caused a recovery of NADH intensity, indicating that the observed changes are reversible. We next grouped all detected photons from mitochondria to form histograms of photon arrival times from NADH autofluorescence for each time point (Fig 1a. lower). We fit the histograms using a model in which the NADH fluorescence decay, $\mathrm{F}(\tau)$, is described by the sum of two exponentials, $\mathrm{F}(\tau) = \mathrm{f} \cdot \exp\left(-\frac{\tau}{\tau_l}\right) + (1-\mathrm{f}) \cdot \exp\left(-\frac{\tau}{\tau_s}\right)$, where $\tau_l$ and $\tau_s$ are long and short fluorescence lifetimes, corresponding to enzyme-bound NADH and freely-diffusing NADH, respectively, and f is the fraction of enzyme-bound NADH[16-17] (Methods).

We repeated the oxygen drop experiments for a total of 68 oocytes. We approximated the slow decrease in oxygen levels as quasistatic, and averaged data from all oocytes to determine how mitochondrial NADH intensity, *I*, lifetimes, $\tau_l$ and $\tau_s$, and the fraction of enzyme-bound NADH, f, varied with oxygen level (Figure 1c). We next calibrated the *in vivo* measured intensity by comparison with *in vitro* measures of known concentrations of NADH, and used the experimentally measured long and short lifetimes to correct for the difference in molecular brightness between free and bound NADH, to determine how the concentration of free NADH, $[NADH_f]$, and enzyme-bound NADH, $[NADH_b]$, depended on oxygen level (Figure 1c, lower right; see methods). $[NADH_f]$ increased as oxygen fell below ~10 μM, while $[NADH_b]$ did not vary with oxygen level.

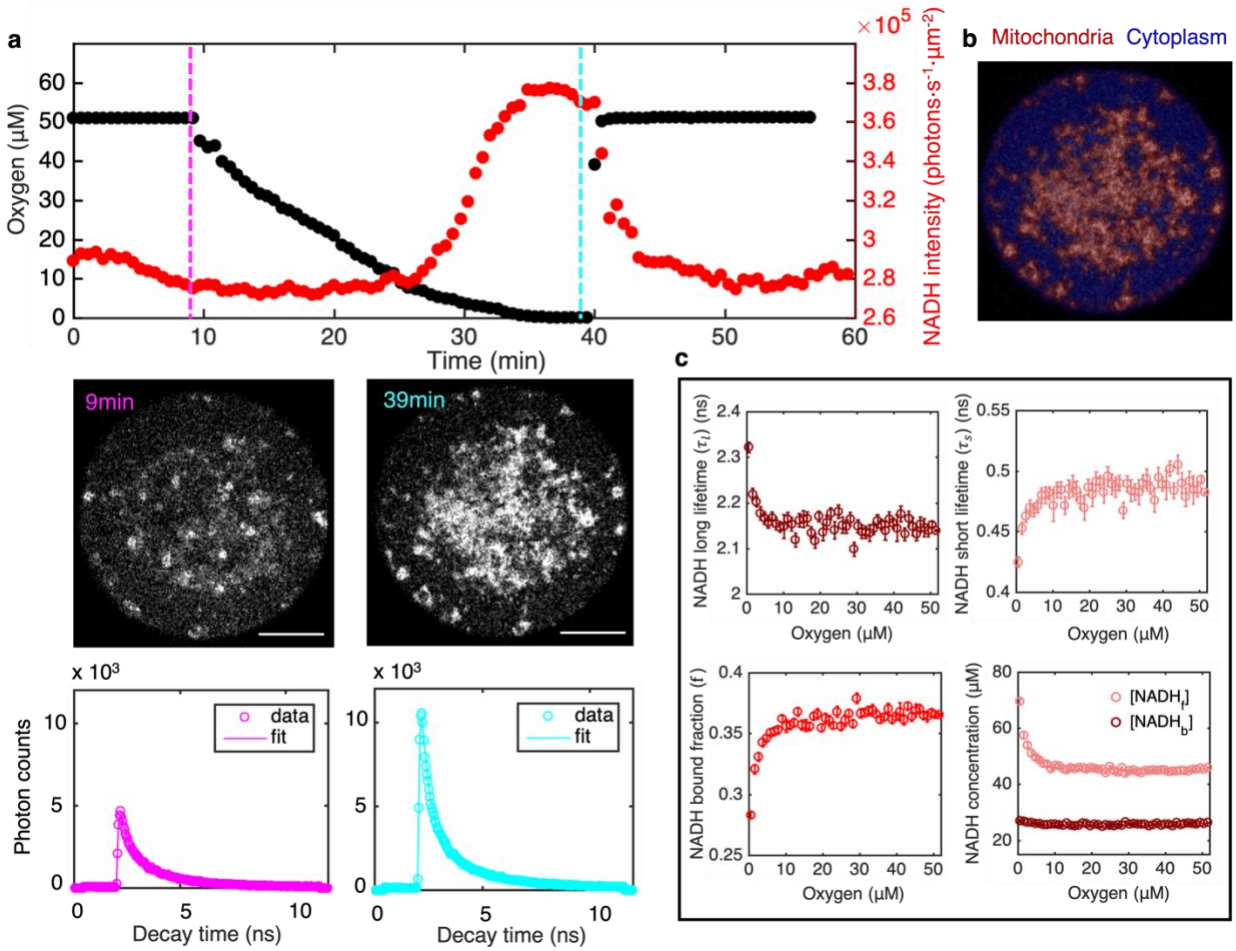


**Figure 1 | FLIM measurements of the response of mitochondrial NADH as a function of oxygen level. a**, Top row: oxygen level (black circles) and mitochondrial NADH intensity (red circles) as a function of time. Middle row: NADH intensity images of MII mouse oocyte at high and low oxygen levels corresponding to times indicated by the vertical lines. Scale bar, 20μm. Bottom row: FLIM decay curves of the corresponding oocyte at low and high oxygen levels, with corresponding fits. **b**, NADH-intensity-based segmentation of mitochondria and cytoplasm. **c**, Mitochondrial NADH long fluorescence lifetime $\tau_l$ (upper left), short fluorescence lifetime $\tau_s$ (upper right), and bound fraction $f$ (lower left) as a function of oxygen level (n=68 oocytes). These FLIM parameters can be used in combination with intensity, $I$, and proper calibration, to obtain the concentration of free NADH, $[NADH_f]$, and the concentration of enzyme-bound NADH, $[NADH_b]$, in mitochondria as a function of oxygen (lower right). Error bars are standard error of the mean (s.e.m).

## Accurately predicting mitochondrial metabolic flux from FLIM of NADH using the NADH redox model

We next developed a mathematical model of NADH redox reactions in order to better interpret these quantitative FLIM measurements. We coarse-grain the TCA into a single effective enzyme that reduces $NAD^+$ to NADH, we coarse-grain the ETC into a single effective enzyme that oxidizes NADH to $NAD^+$, and we explicitly consider the binding and unbinding of NADH and $NAD^+$ to the enzymes in those pathways (Figure 2a). Thus, this model describes the NADH redox cycle, in which NADH can be bound to the oxidizing enzymes of the ETC, $NADH \cdot ox$, or to the reducing enzymes of the TCA, $NADH \cdot re$, or can be in a freely diffusing state, $NADH_f$. Hence, the concentration of NADH bound to enzymes is, $[NADH_b] = [NADH \cdot ox] + [NADH \cdot re]$, and the

total concentration of NADH is, $[NADH] = [NADH_b] + [NADH_f]$. The kinetics of the ETC and TCA are represented by the forward, $r_{ox}^{+}$, and reverse, $r_{ox}^{-}$, oxidation rates of the ETC, and the forward, $r_{re}^{+}$, and reverse, $r_{re}^{-}$, reduction rates of the TCA. The model also includes eight rate constants that characterize the binding and unbinding rates of NADH and $NAD^+$ to the enzymes of the ETC and TCA. This coarse-grained NADH redox model can be explicitly connected to previously developed detailed models of mitochondrial energy metabolism[37-41] (Supp Info Table S1).

Our key result, is that this NADH redox model predicts that the flux through the ETC can be written as (Supp Info):

$$J_{ox} \equiv r_{ox}^{+}[NADH \cdot ox] - r_{ox}^{-}[NAD^{+} \cdot ox] = \tilde{r}_{ox}\left[NADH_f\right] \qquad (1)$$

where $\tilde{r}_{ox} = \alpha(\beta - \beta_{eq})$. $\tilde{r}_{ox}$, the effective oxidation rate of free NADH, is proportional to the difference between the NADH bound ratio, $\beta = \mathrm{f}/(1-\mathrm{f})$, and the equilibrium NADH bound ratio, $\beta_{eq}$ (i.e. what the bound ratio would be if there was no net flux through the ETC), with a constant of proportionality, $\alpha$, that is independent of the reaction rates of the ETC or TCA. Thus, this model shows that there is a direct connection between quantities that can be measured by FLIM of NADH in mitochondria ($\beta$ and $\left[NADH_f\right]$) and the flux through the ETC ($J_{ox}$). This relation holds even if all of the reaction rates, and binding and unbinding rates, are arbitrary (non-linear) functions of metabolite concentrations, enzyme concentrations, and other variables (i.e. membrane potential, oxygen concentration, etc.). The key assumption is that the redox reactions, and binding and unbinding processes, can be approximated as being at steady-state (i.e. undergoing only quasistatic changes over perturbations or development), which is valid under nearly all circumstances of biological interest.

Equation 1 suggests a procedure for using FLIM to infer flux through the ETC: if a condition can be found under which there is no net flux through the ETC, then $\beta_{eq}$ can be measured with FLIM. Once $\beta_{eq}$ is known, then subsequent FLIM measurements of $\beta$ under other conditions allows $\tilde{r}_{ox}$, and hence $J_{ox}$, to be inferred (up to a constant of proportionality). We applied this procedure to analyze our oxygen drop experiments (Figure 1) by assuming that there was no net flux through the ETC at the lowest oxygen level achieved for each oocyte (implying that the measured value of $\beta$ at that oxygen concentration corresponds to $\beta_{eq}$ for that oocyte). This allowed us to obtain a prediction for $J_{ox}$ as a function of oxygen concentration for the oocytes (Figure 2b). To test these predictions, we directly determined $J_{ox}$ as a function of oxygen concentration by measuring the oxygen consumption rate (OCR) of the oocytes using a nanorespirometer[23] (Methods). The direct measurements of $J_{ox}$ from OCR quantitatively agrees with the predictions of $J_{ox}$ from FLIM for all oxygen concentrations (Figure 2b), strongly arguing for the validity of the inference procedure.

We next explored the impact of other perturbations. We first exposed oocytes to sodium oxamate, an inhibitor of lactate dehydrogenase (LDH), which resulted in large changes in the autoflourescence of NADH in mitochondria, including a 29% ± 2% decrease in intensity and a 10% ± 3% increase in bound ratio (Figure 2c). We dropped oxygen levels to determine $\beta_{eq}$, and applied Equation 1 to infer the impact of sodium oxamate on $J_{ox}$ at 50 μM oxygen (i.e. control levels of oxygen). Surprisingly, this procedure revealed that while the addition of sodium oxamate greatly impacts FLIM parameters, it is predicted to not affect $J_{ox}$ (p = 0.94), which was confirmed by

direct measurements of oocytes' OCR (Figure 2c; p = 0.90). We next exposed oocytes to FCCP and repeated the procedure to use FLIM measurements to infer $J_{ox}$. This resulted in a predicted 32% ± 7% increase in $J_{ox}$ from the addition of FCCP, a result which is statistically indistinguishable from the 37% ± 11% increase measured by OCR (Figure 2d; p = 0.78). The quantitative agreement between predictions from FLIM and direct measurements from OCR under a variety of conditions (i.e. varying oxygen tension, sodium oxamate, and FCCP), demonstrates that Equation 1 can be successfully used to infer flux through the ETC.

The work described above used the relation $\tilde{r}_{ox} = \alpha(\beta - \beta_{eq})$ to predict the flux through the ETC. We next show that the model also predicts a relationship between $\tilde{r}_{ox}$ and the fluorescence lifetime of enzyme-bound NADH, $\tau_l$, in mitochondria. This provides a second means to use the model to infer $\tilde{r}_{ox}$, and hence $J_{ox}$, from FLIM of NADH. Specifically, we assume that NADH bound to enzymes of the ETC have a different average lifetime, $\tau_{ox}$, than NADH bound to enzymes of the TCA, $\tau_{re}$, which is reasonable because NADH bound to different enzymes do exhibit different fluorescence lifetimes[15]. This assumption implies that the experimentally measured long lifetime of NADH in mitochondria, $\tau_l$ , is a weighted sum of these two lifetimes, $\tau_l = \tau_{ox}\frac{[NADH{\cdot}ox]}{[NADH{\cdot}ox]+[NADH{\cdot}re]} + \tau_{re}\frac{[NADH{\cdot}re]}{[NADH{\cdot}ox]+[NADH{\cdot}re]}$. This, in turn, leads to a non-trivial prediction of the NADH redox model: that $\tau_l$ is linearly related to $1/\beta$ (Supp Info). Such a linear relationship is indeed observed in individual oocytes subject to oxygen drops (Figure 2e). Experimentally measuring the slope and offset between $\tau_l$ and $1/\beta$, which vary under different conditions (Figure 2e), provides a second means to infer $\tilde{r}_{ox}$ from FLIM measurements (Supp Info). We next used the lifetime ($\tau_l$) method and the bound ratio ($\beta$) method to separately infer $\tilde{r}_{ox}$, and hence $J_{ox}$, in oocytes subject to a wide variety of conditions (varying oxygen levels, varying pyruvate levels, with sodium oxamate, FCCP, rotenone, and oligomycin). The two methods quantitatively agree under all conditions (Figure 2f, p = 0.98), which is a strong self-consistency check that further supports the use of FLIM for inference of flux through the ETC.

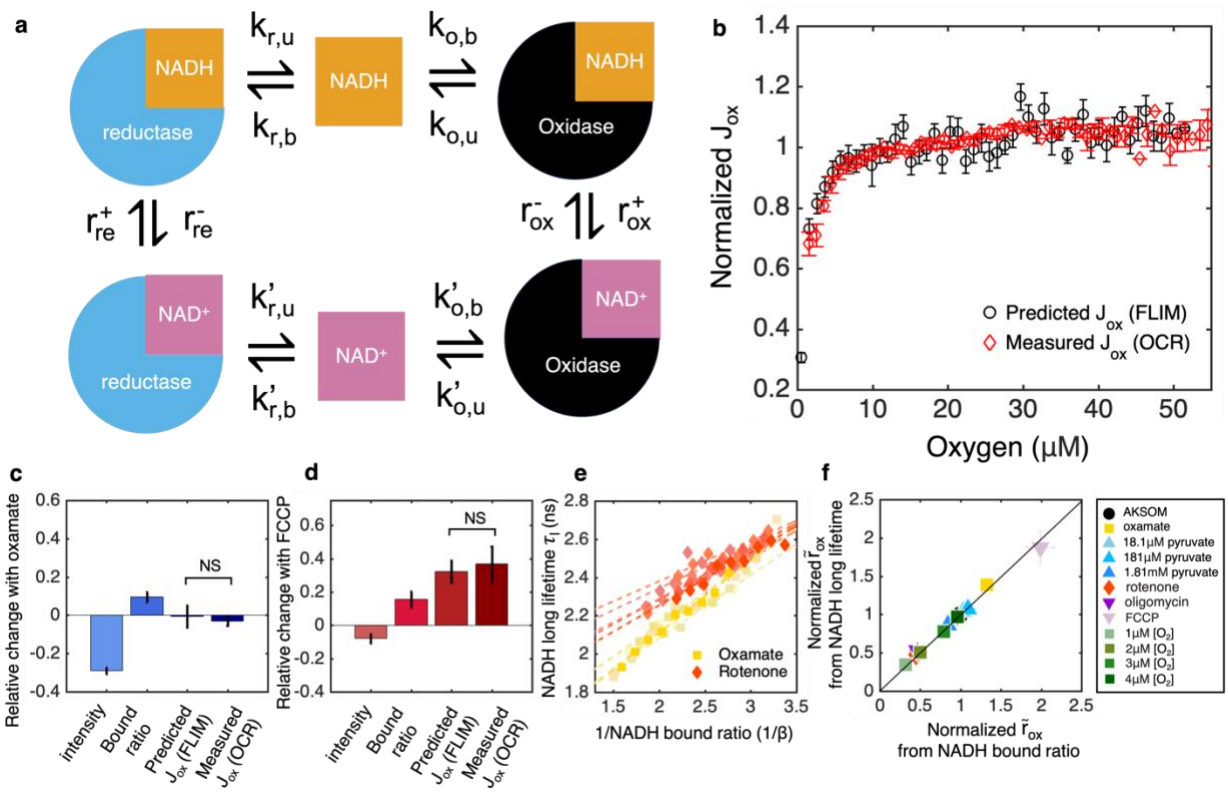


**Figure 2 | NADH redox model enables accurate prediction of flux through the ETC from FLIM measurements of NADH. a**, Schematic of the NADH redox model. Oxidation and reduction pathways of NADH are coarse-grained into two effective enzymes: oxidase (o) and reductase (r), respectively. $r_{ox}^{+}$ and $r_{ox}^{-}$ are the forward and reverse NADH oxidation rates of ETC, and $r_{re}^{+}$ and $r_{re}^{-}$ are the forward and reverse NADH reduction rates of TCA. NADH and its oxidized counterpart $NAD^{+}$ can bind (b) and unbind (u) with the two effective enzymes, which together with the oxidation and reduction reactions, form a redox cycle at steady state with a constant net flux $J_{ox}$. **b**, Predicted flux through the ETC, $J_{ox}$, from the FLIM of NADH (n=68 oocytes) agrees quantitatively with $J_{ox}$ from oxygen consumption rate (OCR) measurements (N=3 measurements, n=15 oocytes per measurement) for all oxygen concentrations. $J_{ox}$ is normalized by its value at 50μM oxygen. **c-d**, relative changes in NADH intensity, bound ratio, predicted $J_{ox}$ from FLIM and measured $J_{ox}$ from OCR with perturbations of oxamate (n=20, N=2) and FCCP (n=28, N=2). Relative changes are calculated as the change of the quantity as a result of the perturbation normalized by the value of the quantify before the perturbation. Predicted $J_{ox}$ agrees with measured $J_{ox}$ in both cases (NS: p>0.05 from two-sided two-sample t-test. p=0.90 (c) and p=0.78 (d)). **e**, NADH long lifetime, $\tau_l$, is linearly related to the inverse of NADH bound ratio, $1/\beta$, from the oxygen drop experiment of individual oocytes treated with oxamate and rotenone (results from 5 representative oocytes are shown for each condition). Each shade corresponds to results from an individual oocyte (symbols are experimental measurements and dashed lines are linear fits). **f**, NADH effective oxidation rate $\tilde{r}_{ox}$ obtained from NADH long lifetime agrees quantitatively with that from NADH bound ratio across all perturbations (p=0.98). $\tilde{r}_{ox}$ is normalized by its value in the AKSOM condition without perturbations. Error bars represent standard error of the mean (s.e.m).

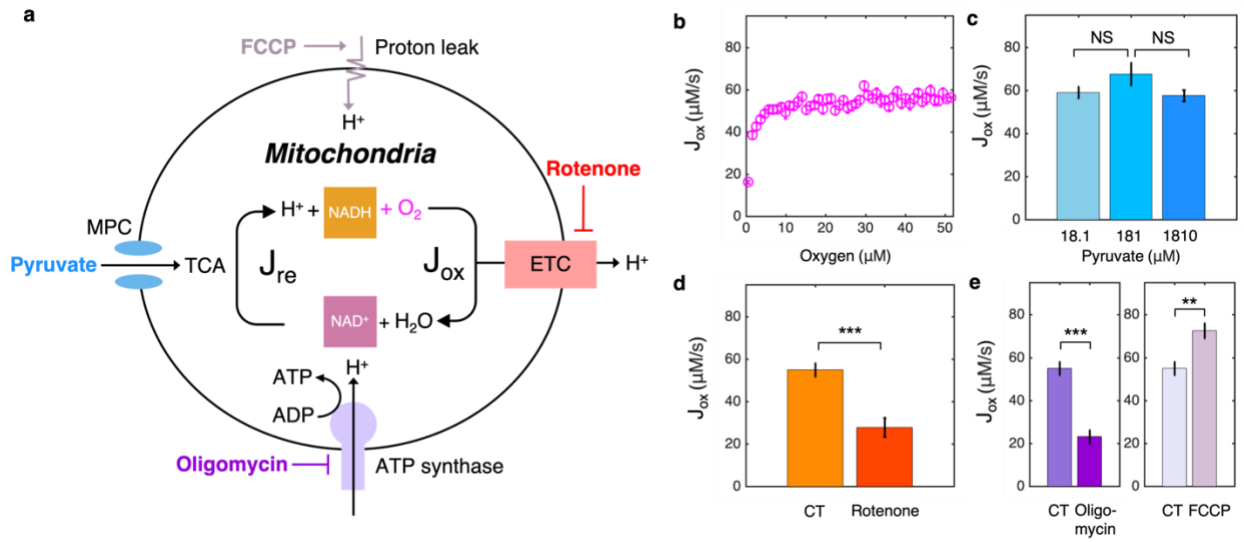


**Figure 3 | Response of ETC flux to mitochondrial perturbations as inferred from FLIM of NADH. a**, schematic of mitochondrial metabolism with biochemical perturbations. NADH redox cycle is composed of the ETC and TCA in mitochondria, where $J_{ox}$ and $J_{re}$ are the net metabolic fluxes through the ETC and TCA for NADH and $NAD^+$, respectively. At steady state, $J_{ox} = J_{re}$. **b-e**, inferred ETC flux in response to oxygen (n=68), pyruvate (n=10,11,15, from low to high concentrations), rotenone (n=15), oligomycin (n=13) and FCCP (n=28) perturbations. CT is AKSOM with oxamate (n=20). n is the number of oocytes. Error bars represent standard error of the mean (s.e.m). NS: p>0.05, ***: p<0.001, **: p<0.01 from two-sided two-sample t-test.

As described above, FLIM of NADH can be used to infer the effective oxidation rate of free NADH because $\tilde{r}_{ox} = \alpha(\beta - \beta_{eq})$, but the constant of proportionality cannot be determined by FLIM alone. Therefore, the redox model allows FLIM measurements to be used to quantitatively measure relative changes in flux through the ETC. If a separate measurement of flux through the ETC can be obtained at one condition, then the inferred relative changes from FLIM can be converted to absolute measurements. We used oocytes cultured in AKSOM media at 50±2 μM oxygen as a reference state, which, from our OCR measurements yielded $J_{ox} = 56.6 \pm 2.0 \mu M \cdot s^{-1}$ and hence a constant of proportionality between $\tilde{r}_{ox}$ and $(\beta - \beta_{eq})$ of $\alpha = 5.4 \pm 0.2 s^{-1}$. Using this value of $\alpha$, we converted our measurements of relative changes in $\tilde{r}_{ox}$ under different conditions (Figure 2f) to absolute values of $\tilde{r}_{ox}$ (Figure S4) and absolute values of $J_{ox}$ (Figure 3). Note that $J_{ox}$ is a flux density with units of concentration per second. Multiplying $J_{ox}$ by the volume of mitochondria in an oocyte gives the total ETC flux in that oocyte. The resulting inferred changes in $J_{ox}$ from FLIM are consistent with expectations (Figure 3b-e). $J_{ox}$ is reduced upon decreasing oxygen level (oxygen is required to run the ETC), upon adding rotenone (which inhibits complex I of the ETC), and upon adding oligomycin (which inhibits ATP synthase and thereby hyperpolarizes mitochondria). $J_{ox}$ increases when FCCP is added (which depolarizes mitochondria). $J_{ox}$ is independent of pyruvate concentrations.

## Revealing a subcellular spatial gradient of mitochondrial metabolic flux in mouse oocytes

Our results presented so far comparing the predicted mitochondrial metabolic flux from FLIM with the directly measured mitochondrial metabolic flux from OCR were performed by averaging together FLIM measurements from all mitochondria within an oocyte (Figures 2 and 3). However, FLIM data is acquired with optical resolution, enabling detailed subcellular measurements. To see if there are spatial variations in FLIM measurements within individual oocytes, we computed the

mean decay time of NADH for each mitochondrial pixel. The NADH decay times display a clear spatial gradient, with higher values closer to the oocyte center (Figure 4a).

To quantify this gradient in more detail, we partitioned mouse oocytes with equal-spaced concentric rings (Figure 4b), and fitted photon decay curves from mitochondrial pixels within each ring to obtain FLIM parameters as a function of distance from the oocyte center. NADH intensity, bound ratio and long lifetime in mitochondria all display significant spatial gradient within oocytes (Figure 4c). To further explore spatial variations in mitochondria in mouse oocytes, we next used the membrane potential-sensitive dye TMRM, which preferentially accumulates in mitochondria with higher membrane potential[42]. We observed a strong spatial gradient of the intensity of TMRM in mitochondria within oocytes, with dimmer mitochondria near the cell periphery (Figure 4d, e), indicating that mitochondria near the periphery of the oocyte have a lower membrane potential. This result is robust to locally normalizing TMRM intensity by mitochondrial mass using a membrane insensitive dye (Mitotracker Red FM), or using an alternative membrane potential-sensitive dye, JC-1 (Figure S5).

Next, using eqn. 1 and $\beta_{eq}$ obtained at the lowest oxygen level, and confirming that $\beta_{eq}$ is uniform within the oocyte with complete inhibition of ETC using rotenone (Figure S6), we predicted the ETC flux, $J_{ox}$, as a function of distance from the oocyte's center. The mitochondrial flux displayed a strong spatial gradient within oocytes, with a higher flux closer to the cell periphery (Figure 4f). Plotting the predicted mitochondrial metabolic flux vs TMRM intensity shows a strong negative correlation between these two variables (Figure 4g), indicating that mitochondrial metabolic flux increases with decreasing mitochondrial membrane potential throughout oocytes. Interestingly, a similar trend is observed upon inhibiting ATP-synthase, which decreases flux (Figure 3e, oligomycin) and increases membrane potential[1], or enhancing proton leak, which increases flux (Figure 3e, FCCP) and decreases membrane potential[1]. Thus, the subcellular spatial variation in mitochondrial metabolic flux that we discovered (Figure 4f) might be caused by spatially varying ATP-synthesis or proton leak in mitochondria in mouse oocytes.

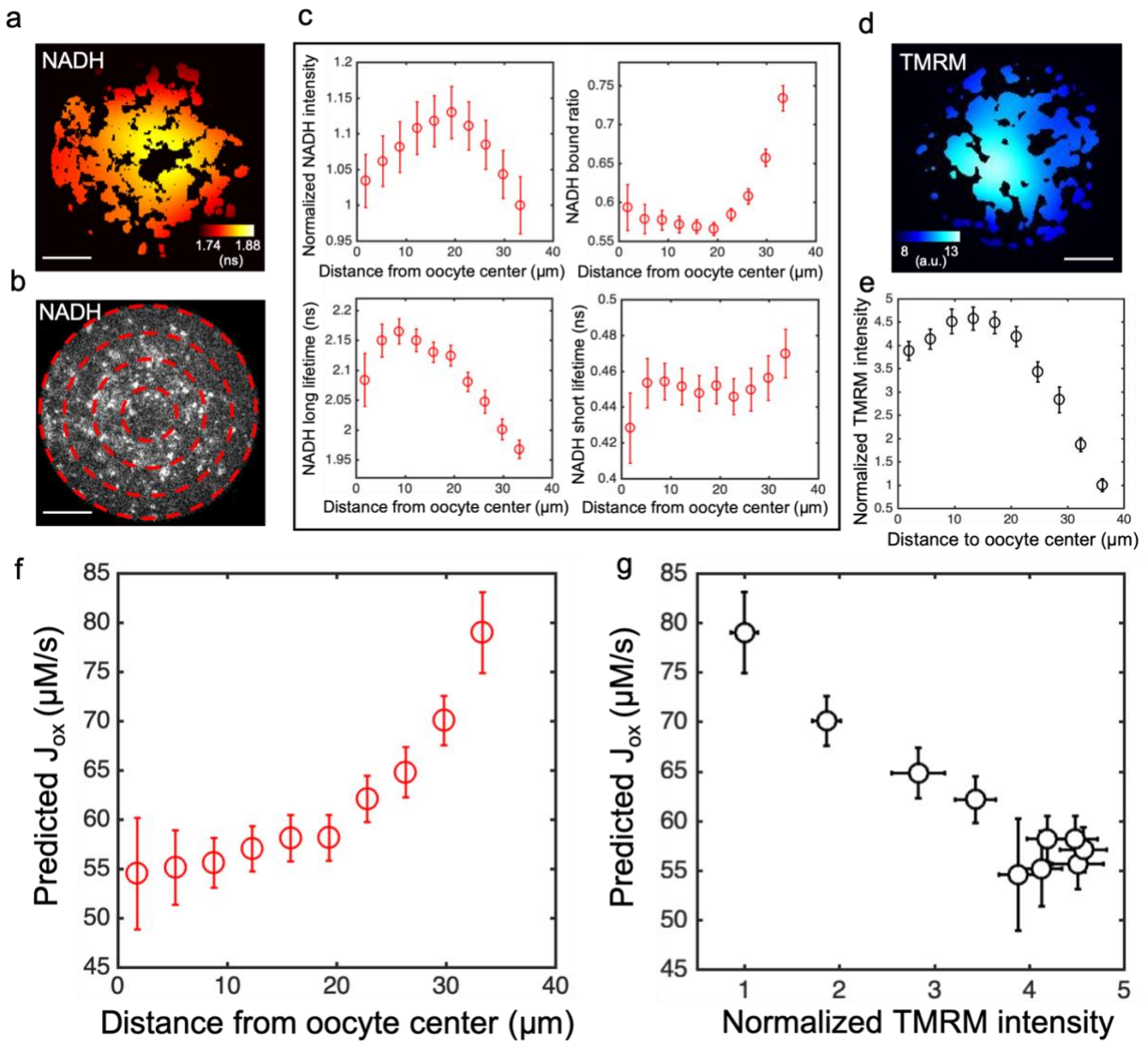


**Figure 4 | Subcellular spatial gradient of mitochondrial metabolism in mouse oocytes. a,** Heatmap of the mean NADH decay time in mitochondria exhibits a subcellular spatial gradient within oocytes. **b,** NADH intensity image of the oocyte partitioned with equal-spaced concentric rings. **c,** Mitochondrial normalized NADH intensity (upper left), bound fraction $f$ (upper right), long fluorescence lifetime $\tau_l$ (lower left), and short fluorescence lifetime $\tau_s$ (lower right) as a function of distance from the oocyte center (n=67). **d,** Heatmap of the TMRM intensity in mitochondria, which increases with mitochondrial membrane potential, exhibits a subcellular spatial gradient within oocytes (n=16). **e,** Normalized TMRM intensity as a function of distance from the oocyte center. **f,** Predicted mitochondrial ETC flux from FLIM of NADH as a function of distance from the oocyte center (n=67). **g,** Subcellular variation in mitochondrial flux correlates with a corresponding subcellular variation in mitochondrial membrane potential. Scale bar 20μm. Error bars represent standard error of the mean (s.e.m).

## Discussion

Despite extensive studies and applications of FLIM in metabolic research[10-18], it has been unclear how to relate FLIM measurements to the activities of the underlying metabolic pathways in cells. We overcome this challenge by developing a coarse-grained NADH redox model to relate FLIM measurements to mitochondrial metabolic fluxes. The model is based on a coarse-grained

description of the NADH redox cycle, and is valid even if all of the reaction rates, and binding and unbinding rates, are arbitrary functions of metabolite concentrations, enzyme concentrations, and other variables (such as membrane potential, oxygen concentration, and the presence of added drugs). This model can be used to infer metabolic fluxes dynamically in living cells, with subcellular resolution, from FLIM measurements of NADH.

Hence, this is a generic method to infer mitochondrial metabolic fluxes across a wide variety of biological samples, including isolated mitochondria, individual cells, and tissues. This technique can also be used to measure spatial variations of metabolic fluxes between cells or even within a single cell, which is not measurable with alternative existing techniques, and will help reveal metabolic heterogeneities[25-26] that otherwise remain hidden on a population level. Applying this approach to mitochondria in mouse oocytes, we accurately predicted the flux through the ETC under a wide variety of biochemical perturbations and discovered subcellular spatial gradients of mitochondrial metabolic fluxes. In this method, the ETC flux is decomposed into the product of the effective oxidation rate and concentration of free NADH. We have explicitly connected the effective oxidation rate of free NADH to those predicted by detailed models of the ETC[37-41] (Supp Info Table S1). Hence our inference approach can be used as a guide to develop and test quantitative models of ETC. We expect our work to provide a new framework for studying metabolic control in living cells[43-44], by enabling FLIM data acquired across a wide range of cells and tissues to be analyzed in a unified manner. The method described here may also be helpful for drug screening and diagnosis of metabolic defects in diseases since it provides a non-invasive, label-free means to measure metabolic fluxes. Finally, this work points the way towards a quantitative theory of mitochondrial kinetics in living cells that can be harnessed to study the correlation between mitochondrial dysfunctions and cellular defects in diseases.

## Methods

### Culturing of mouse oocytes

Frozen MII mouse oocytes (Strain B6C3F1) were purchased from EmbryoTech. Oocytes were thawed and cultured in droplets of AKSOM media purchased from Millipore Sigma in plastic petri dish. Mineral oil from VitroLife was applied to cover the droplets to prevent evaporation of the media. Oocytes were then equilibrated in an incubator at 37°C, with 5% $CO_2$ and air saturated oxygen before imaging. For imaging, oocytes were transferred to a 2μl media droplet in a 35mm glass bottom FluoroDish from WPI covered with 400μl oil. The glass bottom dish was placed in an ibidi chamber with temperature and gas control during imaging. Temperature was maintained at 37°C via heated chamber and objective heater. $CO_2$ was maintained at 5% using gas tanks.

### FLIM measurements

Our FLIM system consists of a two-photon confocal microscope with a 40X 1.25NA water immersion Nikon objective, Becker and Hickle Time Correlated Single Photon Counting (TCSPC) acquisition system and a pulsed MaiTai DeepSee Ti:Sapphire laser from Spectra-Physics. NADH autofluorescence was obtained at 750nm excitation wavelength with a 460/50nm emission filter. Laser power at the objective was maintained at 3mW. The scanning area was 512 by 512 pixels

with a pixel size of 420nm. Acquisition time was 30 seconds per frame. A histogram of NADH decay times was obtained at each pixel of the image.

**Oxygen measurement**

Oxygen level was measured in the Ibidi chamber with an electrode-based oxygen sensor (Gaslab). Since the oil layer covering the media droplet was very thin, the oxygen level in the droplet was assumed to be in instant equilibration with the chamber.

**Image and FLIM data analysis**

To separate mitochondrial NADH signal from cytoplasmic signal, we performed machine learning based segmentation algorithms on NADH intensity images. We used the freeware ilastik[36], which implements a supervised learning algorithm for pixel classification. The classifiers were trained to separate mitochondrial pixels from cytoplasmic pixels with a greater than 80% accuracy, as tested by MitoTracker Red FM (Supp Info). We grouped photons from all mitochondrial pixels to obtain a histogram of NADH decay times for each oocyte. To extract the FLIM parameters of NADH bound fraction f, long lifetime $\tau_l$ and short lifetime $\tau_s$, we fitted the histogram with $\mathrm{G} = \mathrm{IRF} * (C_1 F + C_2)$, where $*$ indicates a convolution, and IRF is the instrument response function of the FLIM system, measured using a urea crystal. $\mathrm{F}(\tau) = \mathrm{f} \cdot \exp\left(-\frac{\tau}{\tau_l}\right) + (1 - \mathrm{f}) \cdot \exp\left(-\frac{\tau}{\tau_s}\right)$ is the two-exponential model for the NADH fluorescence decay. $C_1$ is the amplitude of the decay and $C_2$ is the background noise. The fitting was performed with an custom MATLAB code using a Levenberg-Marquardt algorithm. To obtain the intensity, $I$, of mitochondrial NADH, we first measured the average number of photons per mitochondrial pixel, and divided it by the pixel area, 0.185μm$^2$, and pixel scanning time 4.09μs. The flux of ETC is inferred using eqn. 1 for each oocyte. Heatmaps of mean NADH decay times were obtained by computing NADH decay time of each mitochondrial pixel and averaging over neighboring mitochondrial pixels weighted by a gaussian kernel with a standard deviation of 20 pixels. All FLIM measurements were taken from distinct individual oocytes and error bars in all figures of FLIM represent standard error of the mean across different individual oocytes. Number of oocytes is reported with n.

**Metabolic perturbations**

Oxygen drop experiments were performed by mixing nitrogen-balanced 5% $O_2$ gas with 0% $O_2$ gas at different ratios to create a continuous oxygen drop profile. $CO_2$ was maintained at 5%. Oocytes were imaged for 10mins at 5% $O_2$, 30mins during the continuous drop from 5% $O_2$ to approximately 0% $O_2$, and 20mins after quickly returning to 5% $O_2$. Oxygen levels were simultaneously monitored with an electrode-based oxygen sensor in the ibidi chamber. 5% $O_2$ corresponds to ~50μM of oxygen concentration in the culturing media. All the drug perturbations were performed by equilibrating oocytes in the AKSOM media containing the corresponding drug for 15-30mins before the oxygen drop experiments. 9mM sodium oxamate, 15-60μM rotenone, 5-50μM oligomycin and 1-50μM FCCP were used for the perturbations. Pyruvate perturbations were performed by making KSOM media following Cold Spring Harbor Laboratory protocols with varying concentrations of sodium pyruvate. For oligomycin, FCCP, rotenone and pyruvate

perturbations, 9mM of sodium oxamate was also added to the media to suppress cytoplasmic NADH signal for better mitochondrial segmentation. The addition of the oxamate does not change the ETC flux of the mitochondria. All drugs were purchased from Sigma Aldrich. Temperature was maintained at 37°C. Oocytes were selected and assigned to different perturbation groups randomly. Data were also collected in random order for different oocytes.

**Oxygen consumption rate (OCR) measurement**

The oxygen consumption rate of the oocytes was measured using the nanorespirometer from Unisense[23]. A batch of 15 oocytes were placed at the bottom of a glass capillary with a diameter of 0.68mm and a height of 3mm. The capillary well is filled with AKSOM media. After an equilibration time of ~2 hours, a steady state linear oxygen gradient is established in the capillary well due to the balance of oocyte respiration and oxygen diffusion. An electrode-based oxygen sensor (Unisense) is used to measure the oxygen gradient. The oxygen consumption rate is calculated as the product of the oxygen gradient, diffusivity of oxygen in the media, taken to be $3.37 \times 10^{-5} cm^2/s$, and the cross sectional area of the capillary well, which was $0.36 mm^2$. The entire system was enclosed in a custom built chamber with temperature and gas control. Temperature was maintained at 37°C. Oxygen level was continuously varied during oxygen drop experiments, and maintained at the air saturation level for drug and pyruvate perturbations. All OCR measurements were taken from distinct batches of oocytes in groups of 15. Error bars in all figures of OCR represent standard error of the mean across different groups of oocytes normalized by the number of oocytes in each group. Number of oocytes is reported with n. Number of batches is reported with N.

**Mitochondrial membrane potential measurement**

The spatial distribution of mitochondrial membrane potential within oocytes was measured with a potential-sensitive dye TMRM (Sigma Aldrich). Oocytes were cultured in AKSOM with 100nM TMRM for 30 minutes before imaging. Heatmaps of TMRM intensity were obtained by computing photon counts for each mitochondrial pixel and averaging over neighboring mitochondrial pixels weighted by a gaussian kernel with a standard deviation of 20 pixels. To normalize TMRM intensity by mitochondrial mass, we cultured oocytes in AKSOM with 100nM Mitotracker Red FM and 25nM TMRM for 30 minutes before imaging. We also cultured oocytes in AKSOM with 1μg/ml JC-1 dye for 3 hours before imaging.

## References


1. Brand, M.D., Nicholls, D.G., *Assessing mitochondrial dysfunction in cells.* Biochem J. 2011. 435(Pt 2): p.297–312
2. Lin, M.T., Flint Beal, M., *Mitochondrial dysfunction and oxidative stress in neurodegenerative diseases, Nature*, volume 443, pages 787–795 (2006)
3. Wallace, D.C., *Mitochondria and cancer*, Nat Rev Cancer. 2012 Oct; 12(10): 685–698
4. Bratic, A., Larsson, N., *The role of mitochondria in aging, Journal of Clinical Investigation*, 123: 951-957
5. Lowell, B.B., Shulman, G.I., *Mitochondrial Dysfunction and Type 2 Diabetes, Science* 21 Jan 2005: Vol. 307, Issue 5708, pp. 384-387

6. Dumollard, R., Duchen, M., Carroll, J., *The role of mitochondrial function in the oocyte and embryo.* Curr Top Dev Biol, 2007. 77: p. 21-49.
7. Blerkom, J.V., *Mitochondrial function in the human oocyte and embryo and their role in developmental competence.* Mitochandria, 2011. 11: p. 797-813.
8. Yellen G. Fueling thought: *Management of glycolysis and oxidative phosphorylation in neuronal metabolism*. J Cell Biol. 2018 Jul 2;217(7):2235-2246.
9. Mick, E., et al., *Distinct mitochondrial defects trigger the integrated stress response depending on the metabolic state of the cell,* eLife, 2020;9:e49178
10. Becker, W., *Fluorescence lifetime imaging–techniques and applications*. Journal of Microscopy, 2012. 247: p.119–136.
11. Becker, W., *The bh TCSPC Handbook, 8th Edition*, 2019
12. Bird, D.K. et al**.,** *Metabolic Mapping of MCF10A Human Breast Cells via Multiphoton Fluorescence Lifetime Imaging of the Coenzyme NADH***,** Cancer Res 2005 65:8766–8773
13. Skala, M.C. et al., *In vivo Multiphoton Fluorescence Lifetime Imaging of Protein-bound and Free NADH in Normal and Pre-cancerous Epithelia.* J Biomed Opt. 2007 Mar-Apr; 12(2): 024014
14. Heikal, A.A., *Intracellular coenzymes as natural biomarkers for metabolic activities and mitochondrial anomalies*. Biomark Med, 2010. 4(2): p. 241-63.
15. Sharick, J.T., et al., *Protein-bound NAD(P)H Lifetime is Sensitive to Multiple Fates of Glucose Carbon,* Sci Rep., 2018, 8:5456
16. Sanchez, T., et al., *Metabolic imaging with the use of fluorescence lifetime imaging microscopy (FLIM) accurately detects mitochondrial dysfunction in mouse oocytes.* Fertility and Sterility, 2018, 110, 7
17. Sanchez T., et al., *Combined noninvasive metabolic and spindle imaging as potential tools for embryo and oocyte assessment*. Human Reproduction 2019, 1, 13
18. Ma, N. et al., *Label-free assessment of preimplantation embryo quality by the Fluorescence Lifetime Imaging Microscopy (FLIM)-phasor approach.* Scientific Reports 2019, 9, 13206
19. J.G. Salway, *Metabolism at a Glance*, 4th Edition, ISBN: 978-0-470-67471-0, February 2017, Wiley-Blackwell
20. Mitchell, P., *Coupling of Phosphorylation to Electron and Hydrogen Transfer by a Chemi-Osmotic type of Mechanism*, Nature 191, 144-148 (1961)
21. Ferrick DA, Neilson A, Beeson C. *Advances in measuring cellular bioenergetics using extracellular flux.* Drug Discov Today. 2008; 13:268–274.
22. Houghton, F.D., Thompson, J.G., Kennedy, C.J., Leese, H.J., *Oxygen consumption and energy metabolism of the early mouse embryo.* Mol Reprod Dev. 1996.44(4):476-85
23. Lopes, A.S., et al., *Respiration rates of individual bovine in vitro-produced embryos measured with a novel, non-invasive and highly sensitive microsensor system.* Reproduction 2005, 130, 669-679
24. Wiechert, W., *13C Metabolic flux analysis*, Metabolic Engineering, 2001, 3(3), 195-206
25. Takhaveev, V., Heinemann, M., *Metabolic heterogeneity in clonal microbial populations*. Current opinion in microbiology, 2018 Oct; 45:30-38
26. Aryaman, J., Johnston I. G., Jones, N.S., *Mitochondrial Heterogeneity,* Front. Genet., 25 January 2019, 9, 718
27. Saks VA, et al. *Permeabilized cell and skinned fiber techniques in studies of mitochondrial function in vivo*. Mol Cell Biochem. 1998; 184:81–100
28. Perry, S.W., et al., *Mitochondrial membrane potential probes and the proton gradient: a practical usage guide*, Biotechniques. 2011 Feb; 50(2): 98–115
29. Imamura, H., et al., *Visualization of ATP levels inside single living cells with fluorescence resonance energy transfer-based genetically encoded indicators.* Proc Natl Acad Sci USA. 2009. 106(37): p. 15651–15656
30. Berg, J., Hung, Y. P., Yellen, G., *A genetically encoded fluorescent reporter of ATP:ADP ratio*. *Nat. Methods*. 6, 161–166 (2009).
31. Díaz-García, C.M. et al., *Neuronal stimulation triggers neuronal glycolysis and not lactate uptake,* Cell Metab. 2017 Aug 1; 26(2): 361–374.e4

32. Martin, A.S., et al., *Imaging Mitochondrial flux in single cells with a FRET sensor for pyruvate*, PloS ONE, 2014, 9(1): e85780
33. Biggers, J.D., Racowsky, C., *The development of fertilized human ova to the blastocyst stage in KSOMAA medium: is a two-step protocol necessary?* Reprod Biomed Online. 2002 Sep-Oct;5(2):133-40
34. Lane, M., Gardner, D.K., *Lactate Regulates Pyruvate Uptake and Metabolism in the Preimplantation Mouse Embryo,* Biology of Reproduction, Volume 62, Issue 1, 1 January 2000, Pages 16–22
35. Bustamante, S., et al., *Quantifying the cellular NAD+ metabolome using a tandem liquid chromatography mass spectrometry approach,* Metabolomics. 2017 Dec 23; 14(1):15
36. Berg, S., et al., *ilastik: interactive machine learning for (bio)image analysis*, Nature Methods, 16, 1226-1232(2019)
37. Beard D.A., *A biophysical model of the mitochondrial respiratory system and oxidative phosphorylation.* PLoS Comput Biol. 2005. 1(4): e36
38. Korzeniewski, B., Zoladz, J.A., *A model of oxidative phosphorylation in mammalian skeletal muscle*, Biophysical Chemistry, 2001, 92, 17-34
39. Hill, T.L., *Free Energy Transduction in Biology*, (1977) Academic
40. Jin, Q., Bethke, C.M., *Kinetics of Electron Transfer through the Respiratory Chain*, Biophysical Journal, Volume 83, October 2002, 1797–1808
41. Chang, I., Heiske, M., Letellier, T., Wallace, D., Baldi, P., *Modeling of Mitochondria Bioenergetics Using a Composable Chemiosmotic Energy Transduction Rate Law: Theory and Experimental Validation,* PLoS One. 2011;6(9):e14820
42. AL-Zubaidi, U., et al. *The spatio-temporal dynamics of mitochondrial membrane potential during oocyte maturation*, Molecular Human Reproduction, 25(11):695-705(2019)
43. Hafner, R.P., Brown, G.C., Brand, M.D., *Analysis of the control of respiration rate, phosphorylation rate, proton leak rate and protonmotive force in isolated mitochondria using the 'top-down' approach of metabolic control theory***,** Eur J Biochem. 1990 Mar 10;188(2):313-9
44. Chance B., Williams G.R., *respiratory enzymes in oxidative phosphorylation. I. Kinetics of oxygen utilization.* J. Biol. Chem. 1955, 217(1):383-93

## Acknowledgements

We thank Carlos Manlio Díaz-García, Gary Yellen, Peter Foster, Easun Arunachalam, Yu-Chen Chao, Bill Ireland and Denis Titov for suggestions, advice, and comments on the manuscript. This work is supported by the National Institute of Health (R01HD092550-01) and the National Science Foundation (PFI-TT-1827309).

## Author contributions

X.Y. and D.J.N conceptualized the work. X.Y. performed the experiments, modeling and data analysis. X.Y. and D.J.N wrote the manuscript.

# Supplementary Information

## Segmentation of mitochondria

We used Ilastik, a machine-learning-based software for image analysis, to identify pixels in the NADH images containing mitochondria[1]. For each experiment, we generated a time lapse movie of NADH. We used a few images in the movie as the training data set to train the software to identify mitochondrial pixels by manually selecting high brightness pixels in local clusters. We then applied the trained pixel classifier to generate a mitochondrial probability map for each image in the entire movie, with each pixel assigned a probability between 0 to 1 to be mitochondrial pixel. Pixels with a probability higher than 0.7 were considered to be mitochondrial pixels.

To test the accuracy of this segmentation algorithm, we immersed the oocytes in media containing MitoTracker Red FM, a dye that specifically labels mitochondria. Pixels with intensity above 60 percentile in the MitoTracker image were considered to be mitochondrial pixels. We imaged NADH and MitoTracker for the same oocyte and compared the resulting distribution of mitochondria (Figure S1). The accuracy of the NADH-based segmentation of mitochondria is $80.6 \pm 1.0\%$ (SEM) as averaged over 7 oocytes.

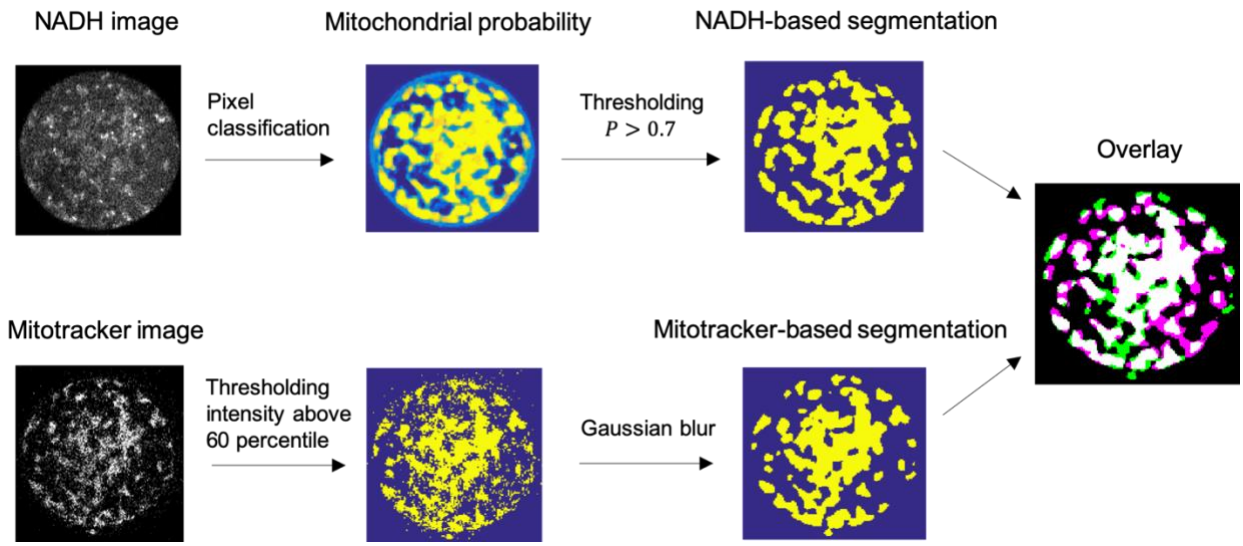


**Figure S1 | Machine learning based segmentation of mitochondria from NADH images.** The NADH-based segmentation image is overlaid with MitoTracker-based segmentation image. The white region corresponds to the overlap. The accuracy of the NADH-based segmentation is quantified as the ratio of the photon count from the overlap pixels to the photon count from mitochondrial pixels based on NADH segmentation.

## Converting NADH intensity to NADH concentrations

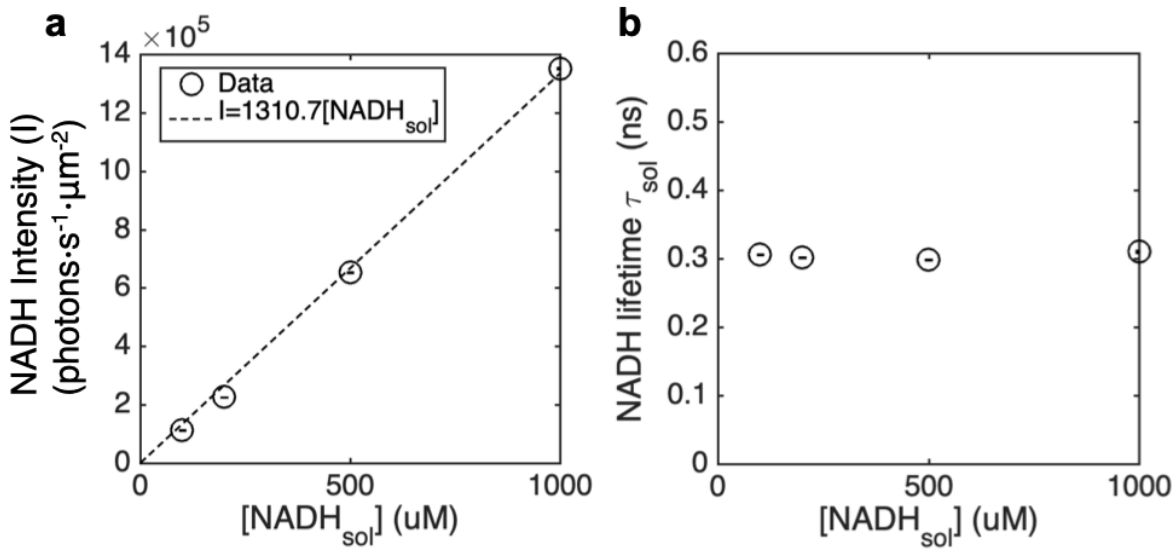


**Figure S2 | *In vitro* calibration and conversion of NADH concentrations from fluorescence intensities. a,** NADH intensity vs titrated NADH concentrations in AKSOM solution. **b,** fluorescence lifetime of NADH in AKSOM solution.

Since the molecular brightness of NADH depends on the fluorescence lifetime of NADH, which changes drastically upon binding enzymes, the NADH concentration is not linearly proportional to NADH intensity. FLIM provides an accurate way of measuring NADH concentrations by simultaneously measuring fluorescence intensity and lifetime. We now derive the NADH intensity-concentration relation from the FLIM measurements. Assuming molecular brightness is proportional to the fluorescence lifetime, and therefore that free and bound NADH have different contributions to the measured intensity, we have

$$I = c_s\tau_s\left[NADH_f\right] + c_s\tau_l[NADH_b]\ (S1),$$

where $I$ is the intensity of NADH and $c_s$ is a calibration factor that depends on the laser power. From eqn. (S1), we obtained the concentrations of free and bound NADH:

$$\left[NADH_f\right] = \frac{I(1-f)}{c_s[(\tau_l-\tau_s)f+\tau_s]}\ (S2),$$
$$[NADH_b] = \left[NADH_f\right]\frac{f}{1-f}\ (S3),$$

where $f$ is the fraction of bound NADH.

To get the calibration factor $c_s$, we titrated NADH in AKSOM solutions and fitted the calibration curve using:

$$I = c_s\tau_{sol}[NADH_{sol}]\ (S4),$$

where $\tau_{sol}$ is the lifetime of NADH in solution. $\tau_{sol}$ was directly measured by FLIM (Fig. S2b), allowing us to obtain $c_s$ from the fit (Fig. S2a). Using eqns. (S2)-(S3), we obtained the free and bound NADH concentrations in mouse oocytes for oxygen drop (Fig. 1c in the main text) and drug perturbations (Fig. S3e-f).

**The NADH redox model**

We start with the equations characterizing the dynamics of the NADH redox model as described in Fig. 2a in the main text:

$$\frac{d[NADH\cdot re]}{dt} = k_{r,b}[NADH_f] - k_{r,u}[NADH\cdot re] + r_{re}^{+}[NAD^{+}\cdot re] - r_{re}^{-}[NADH\cdot re] \text{ (S5)},$$
$$\frac{d[NADH_f]}{dt} = k_{r,u}[NADH\cdot re] + k_{o,u}[NADH\cdot ox] - k_{r,b}[NADH_f] - k_{o,b}[NADH_f] \text{ (S6)},$$
$$\frac{d[NADH\cdot ox]}{dt} = k_{o,b}\left[NADH_f\right] - k_{o,u}[NADH\cdot ox] - r_{ox}^{+}[NADH\cdot ox] + r_{ox}^{-}[NAD^{+}\cdot ox] \text{ (S7)},$$
$$\frac{d[NAD^{+}\cdot ox]}{dt} = k'_{o,b}[NAD_f^{+}] - k'_{o,u}[NAD^{+}\cdot ox] + r_{ox}^{+}[NADH\cdot ox] - r_{ox}^{-}[NAD^{+}\cdot ox] \text{ (S8)},$$
$$\frac{d[NAD_f^{+}]}{dt} = k'_{r,u}[NAD^{+}\cdot re] + k'_{o,u}[NAD^{+}\cdot ox] - k'_{r,b}[NAD_f^{+}] - k'_{o,b}[NAD_f^{+}] \text{ (S9)},$$
$$\frac{d[NAD^{+}\cdot re]}{dt} = k'_{r,b}[NAD_f^{+}] - k'_{r,u}[NAD^{+}\cdot re] - r_{re}^{+}[NAD^{+}\cdot re] + r_{re}^{-}[NADH\cdot re] \text{(S10)},$$

where $[NADH_f]$ and $[NAD_f^{+}]$ are the concentrations of free NADH and free $NAD^{+}$; $[NADH\cdot re]$ and $[NAD^{+}\cdot re]$ are concentrations of reductase-bound NADH and $NAD^{+}$; $[NADH\cdot ox]$ and $[NAD^{+}\cdot ox]$ are concentrations of oxidase-bound NADH and $NAD^{+}$; $k$ denotes binding (b) and unbinding (u) rates, with subscript r and o denoting reductase and oxidase, respectively; $r_{re}^{+}$ and $r_{re}^{-}$ are the forward and reverse reaction rates of the reductase in the TCA; $r_{ox}^{+}$ and $r_{ox}^{-}$ are the forward and reverse reaction rates of the oxidase in the ETC. The reaction rates, and binding and unbinding rates, can be arbitrary functions of metabolite concentrations, enzyme concentrations, and other variables (such as membrane potential, oxygen concentration, and the presence of added drugs).

The flux through the ETC is

$$J_{ox} \equiv r_{ox}^{+}[NADH\cdot ox] - r_{ox}^{-}[NAD^{+}\cdot ox] \ (S11).$$

At steady state (or in the quasistatic limit), all the time derivatives are zero. Setting $d[NADH\cdot ox]/dt$ (eqn. (S7)) to zero, we obtained the steady state flux through the ETC:

$$J_{ox} = k_{o,b}\left[NADH_f\right] - k_{o,u}[NADH\cdot ox] \ (S12).$$

Setting $d[NADH_f]/dt$ (eqn. (S6)) to zero gives:

$$\left(k_{o,b} + k_{r,b}\right)\left[NADH_f\right] = k_{o,u}[NADH\cdot ox] + k_{r,u}[NADH\cdot re] \ (S13).$$

and using:

$$[NADH \cdot re] + [NADH \cdot ox] = [NADH_b] \ (S14),$$

from which we solved for $[NADH \cdot ox]$:

$$[NADH \cdot ox] = \frac{k_{r,b}+k_{o,b}}{k_{o,u}-k_{r,u}}\left[NADH_f\right] - \frac{k_{r,u}}{k_{o,u}-k_{r,u}}[NADH_b] \ (S15).$$

Substituting $[NADH \cdot ox]$ in eqn.(S12) with eqn.(S15), we obtained our central result:

$$J_{ox} = \tilde{r}_{ox}\left[NADH_f\right] \ \text{(S16)}.$$

From eqn.(S16) we see that the flux through ETC is a product of the effective oxidation rate of free NADH, $\tilde{r}_{ox}$, and the concentration of free NADH, $\left[NADH_f\right]$, where

$$\tilde{r}_{ox} = \alpha\left(\beta - \beta_{eq}\right) \ \text{(S17)},$$

and

$$\alpha = \frac{k_{o,u}\, k_{r,u}}{k_{o,u} - k_{r,u}} (S18),$$

where we defined the NADH bound ratio and its equilibrium counterpart as:

$$\beta = \frac{[NADH_b]}{\left[NADH_f\right]} \ (S19),$$
$$\beta_{eq} = \beta_{eq}^{ox} + \beta_{eq}^{re} \ (S20),$$
$$\beta_{eq}^{ox} = \frac{k_{o,b}}{k_{o,u}} \ (S21),$$
$$\beta_{eq}^{re} = \frac{k_{r,b}}{k_{r,u}} \ (S22).$$

**Inferring flux through the ETC from FLIM measurements of NADH using the NADH redox model**

Eqn. (S16), or equivalently eqn. 1 from the main text, can be used to infer the flux through the ETC, $J_{ox}$. FLIM measurements of NADH can be used to determine $\beta$, $\beta_{eq}$, and $[NADH_f]$, and thus give $J_{ox}$ up to a constant of proportionality, $\alpha$. If $\alpha$ is independently measured at one condition, then the absolute value of $J_{ox}$ can be determined for all conditions.

Briefly, we measure the NADH bound ratio, $\beta$, using $\beta = \mathrm{f}/(1-\mathrm{f})$, where f is the NADH bound fraction obtained by fitting the fluorescence decay curve of NADH (See Methods). We obtain the equilibrium bound ratio, $\beta_{eq}$, by dropping the oxygen level to the lowest achievable value with our setup, $[O_2] = 0.26 \pm 0.04\ \mu M$ in our experiments. Note that $\beta_{eq}$ changes with culture conditions, and therefore needs to be separately determined for every drug and nutrient perturbation (Fig.S3h). We obtain $[NADH_f]$ from FLIM measurements by using the NADH intensity corrected by fluorescence lifetimes according to eqn. (S2).

We obtain $\alpha$ using direct measurement of $J_{ox}$ from oxygen consumption rate (OCR) measurements:

$$\alpha = \frac{J_{ox}}{(\beta - \beta_{eq})[NADH_f]} = 2\frac{OCR}{(\beta - \beta_{eq})[NADH_f]V_m} \, (S23),$$

where $V_m = 9.5 \times 10^4 \ \mu m^3$ is the average volume of mitochondria per oocyte approximated from the area fraction of mitochondria based on the segmentation, where the mitochondrial area fraction is estimated at 46% and oocyte volume at $2 \times 10^5 \ \mu m^3$. Using $OCR$=2.68$\pm$0.06 fmol/s per oocyte in the AKSOM media at 50μM oxygen level, we get $\alpha = 5.4 \pm 0.2 s^{-1}$.

Once $\alpha$ is calibrated for one condition using eqn. (S23), and $\beta_{eq}$ is determined from an oxygen drop experiment, then subsequent FLIM measurements of $\beta$ and $[NADH_f]$ can be used with eqn. (S16) to determine the absolute value of $J_{ox}$ for all conditions (Figure 3 main text).

**Parameters obtained from FLIM measurements of NADH**

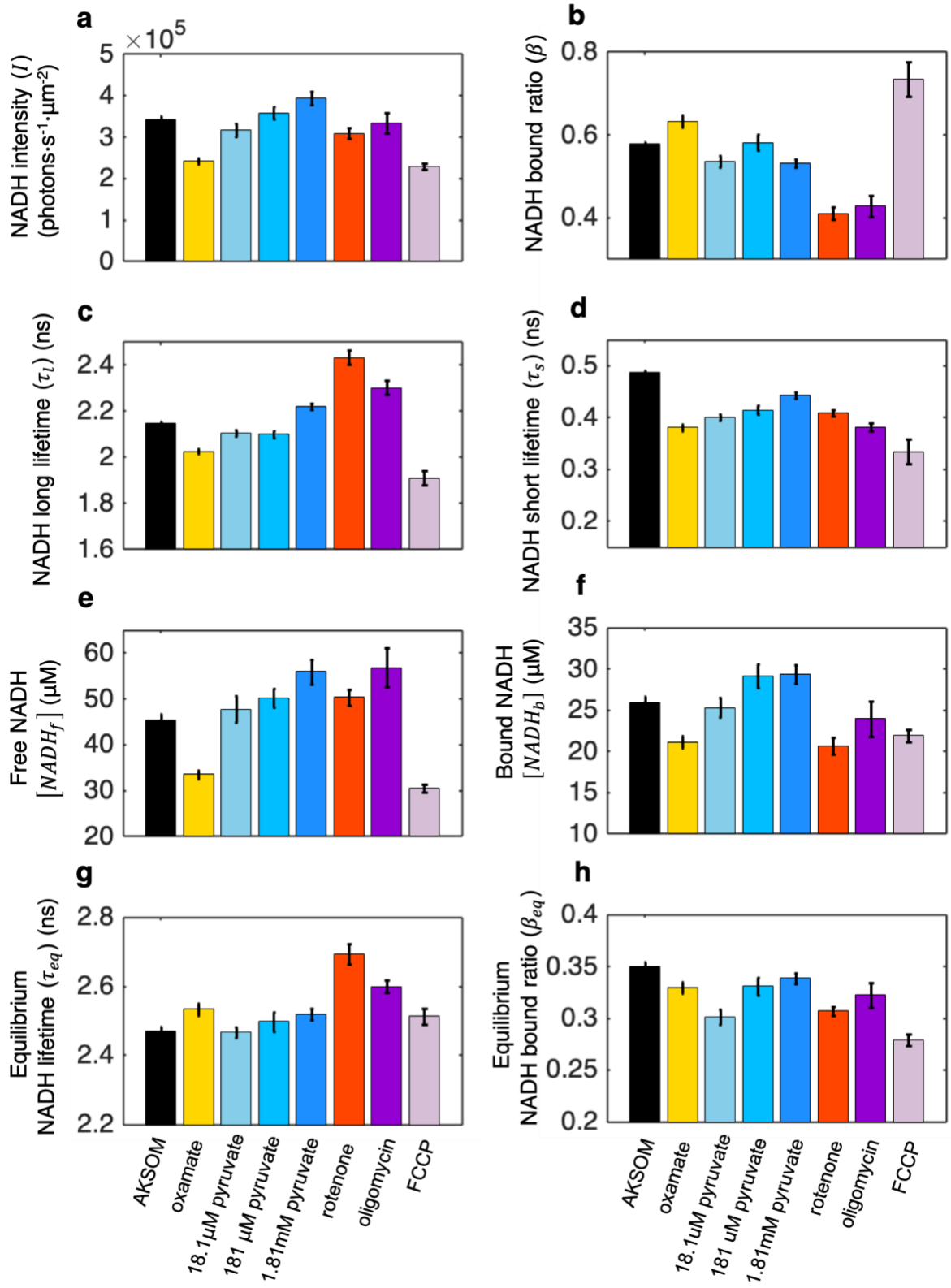

**Figure S3 | Parameters obtained from FLIM measurements of NADH in mitochondria for different biochemical perturbations. a,** NADH intensity. **b-d,** NADH bound ratio and NADH long and short fluorescence lifetimes obtained from fitting FLIM decay curves using the two-exponential decay model (Method). **e-f,** free and bound NADH concentrations obtained by using eqns (S2) and (S3), and the calibration from eqn. (S4). **g-h,** Equilibrium NADH long lifetime and bound ratio, measured at the lowest oxygen level under different conditions. 9mM sodium oxamate was present in all conditions except for AKSOM to suppress the cytoplasmic signal and allow for better mitochondrial segmentation. AKSOM (n=68), oxamate (n=20), pyruvate (n=10, 11, 15, from low to high concentrations), rotenone (n=15), oligomycin (n=13) and FCCP (n=15). n is the number of oocytes. Error bars represent standard error of the mean (s.e.m).

## Inferring effective NADH oxidation rate from NADH long fluorescence lifetime

In this section, we derive an alternative procedure for determining the effective NADH oxidation rate $\tilde{r}_{ox}$, and hence $J_{ox}$ from eqn. (S16), using changes in the NADH long fluorescence lifetime. The NADH long fluorescence lifetime, $\tau_l$, is associated with enzyme-bound NADH[2]. In the NADH redox model described above, and in Fig 2a of the main text, the enzyme-bound NADH consists of reductase-bound NADH ($[NADH \cdot re]$) and oxidase-bound NADH ($[NADH \cdot ox]$). We therefore assume that the experimentally measured NADH long lifetime, $\tau_l$, is a linear combination of the lifetimes of $[NADH \cdot ox]$ and $[NADH \cdot re]$:

$$\tau_l = \tau_{ox} \frac{[NADH \cdot ox]}{[NADH \cdot ox]+[NADH \cdot re]} + \tau_{re} \frac{[NADH \cdot re]}{[NADH \cdot ox]+[NADH \cdot re]} \ (S24),$$

where $\tau_{ox}, \tau_{re}$ are fluorescence lifetimes corresponding to the oxidase-bound NADH and reductase-bound NADH, respectively. Substituting $[NADH \cdot ox]$ and $[NADH \cdot re]$ in eqn. (S24) with $\beta$ using eqns. (S14)-(S15) and eqn. (S19), we derive that the NADH long fluorescence lifetime $\tau_l$ is linearly related to the inverse of the NADH bound ratio $1/\beta$:

$$\tau_l = A\frac{1}{\beta} + B \ (S25),$$

with

$$A = (\tau_{ox} - \tau_{re}) \frac{k_{o,b}+k_{r,b}}{k_{o,u}-k_{r,u}} \ (S26),$$
$$B = \frac{k_{o,u}\tau_{re}-k_{r,u}\tau_{ox}}{k_{o,u}-k_{r,u}} \ (S27),$$

which is empirically observed during oxygen drop experiments, as shown in Fig. 2e of the main text. This self-consistency check argues for the validity of the assumption in eqn. (S24).

At equilibrium, when there is no flux through the ETC (i.e. $J_{ox} = 0$), eqn.$(S25)$ gives:

$$\tau_{eq} = A\frac{1}{\beta_{eq}} + B \ (S28),$$

where $\tau_{eq}$ is the NADH long lifetime at equilibrium. Using eqns. (S25) and (S28) in combination with (S17), we obtain $\tilde{r}_{ox}$ in terms of $\tau_l$:

$$\tilde{r}_{ox} = \alpha \frac{A}{\tau_{eq} - B} \left( \frac{\tau_{eq} - \tau_l}{\tau_l - B} \right) \ (S29),$$

where A and B are the slope and offset of the linear relation between $\tau_l$ and $1/\beta$ in eqn. (S25).

We experimentally measure A and B for each oocyte from the slope and offset of a linear fit between $\tau_l$ and $1/\beta$ during oxygen drop experiments (Fig.2e in the main text; Fig.S4a-b). We obtain the equilibrium long lifetime, $\tau_{eq}$, by FLIM measurements at the lowest achievable oxygen level, $[O_2] = 0.26 \pm 0.04\ \mu M$ in our experiments. Once A, B, and $\tau_{eq}$ are measured, eqns. (S29) can be used to determine $\tilde{r}_{ox}$ from FLIM measurements of $\tau_l$. If $\alpha$ is not known, this procedure can only be used to obtain $\tilde{r}_{ox}$ up to a constant of proportionality. If $\alpha$ is independently measured, as described above, then eqn (S29) can be used to determine the absolute value of $\tilde{r}_{ox}$ (Fig.S4c-f).

As described in the main text, $\tilde{r}_{ox}$ inferred using eqn (S29) produces the same results as $\tilde{r}_{ox}$ inferred using eqn (S17) (Fig. 2f in the main text). The agreement between these two methods is a strong self-consistency check of the model.

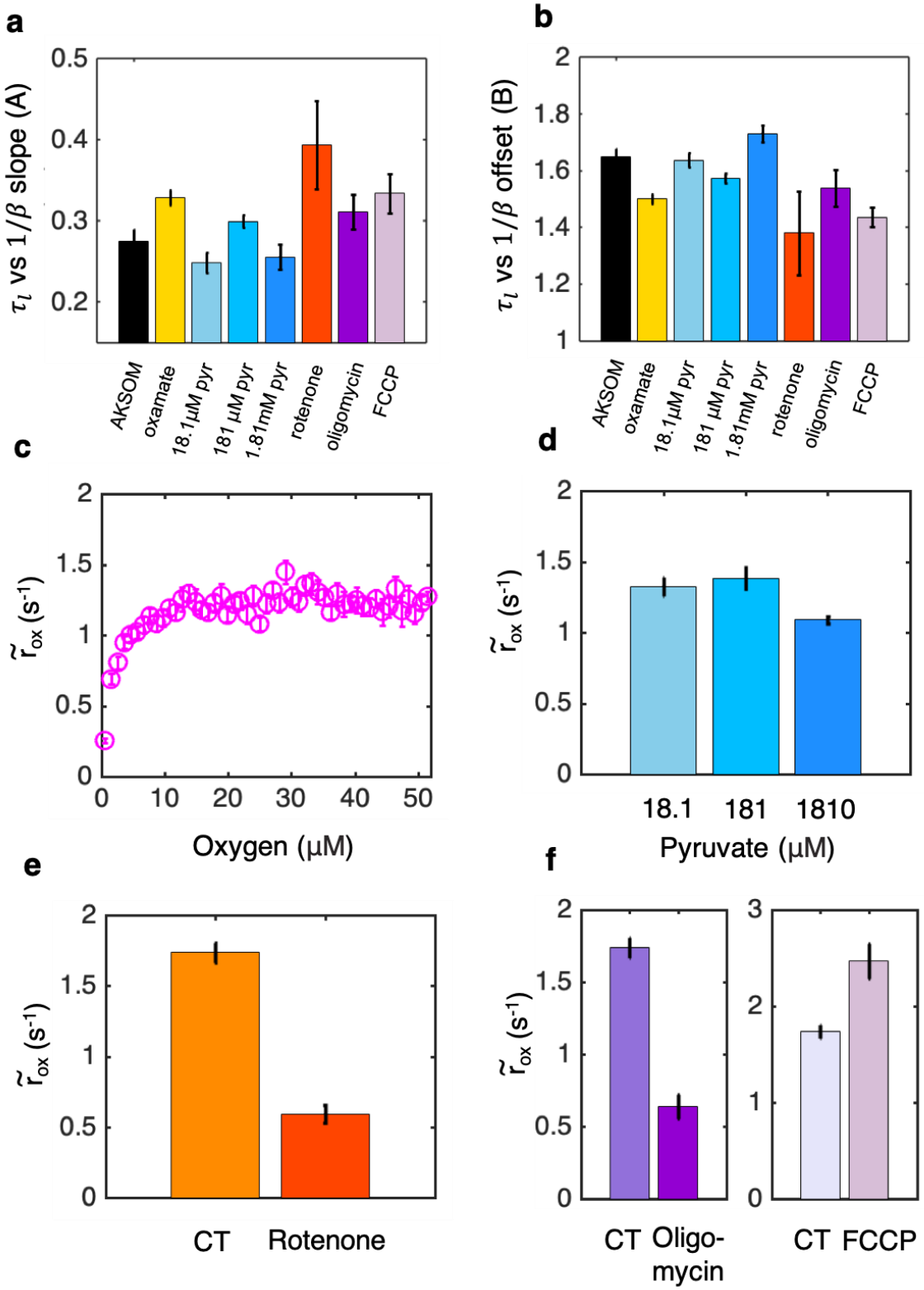
a
$\tau_l$ vs $1/\beta$ slope (A)
0.5
0.4
0.3
0.2
AKSOM
oxamate
18.1μM pyr
181 μM pyr
1.81mM pyr
rotenone
oligomycin
FCCP
b
$\tau_l$ vs $1/\beta$ offset (B)
2
1.8
1.6
1.4
1.2
1
c
$\tilde{r}_{ox}$ (s$^{-1}$)
2
1.5
1
0.5
0
0
10
20
30
40
50
Oxygen (μM)
d
18.1
181
1810
Pyruvate (μM)
e
CT
Rotenone
f
CT
Oligo-
mycin
CT
FCCP

**Figure S4 | Response of the effective oxidation rate of free NADH to mitochondrial perturbations. a-b,** slope (A) and offset (B) obtained by fitting eqn. (S25) to $\tau_l$ vs $1/\beta$ (Fig. 2e in the main text). **c-f**, effective oxidation rate $\tilde{r}_{ox}$ in response to oxygen (n=68), pyruvate (n=10, 11, 15, from low to high concentrations), rotenone (n=15), oligomycin (n=13) and FCCP perturbations (n=15). CT is AKSOM with oxamate (n=20). n is the number of oocytes. Error bars represent standard error of the mean (s.e.m).

## Subcellular spatial gradient of mitochondrial membrane potential

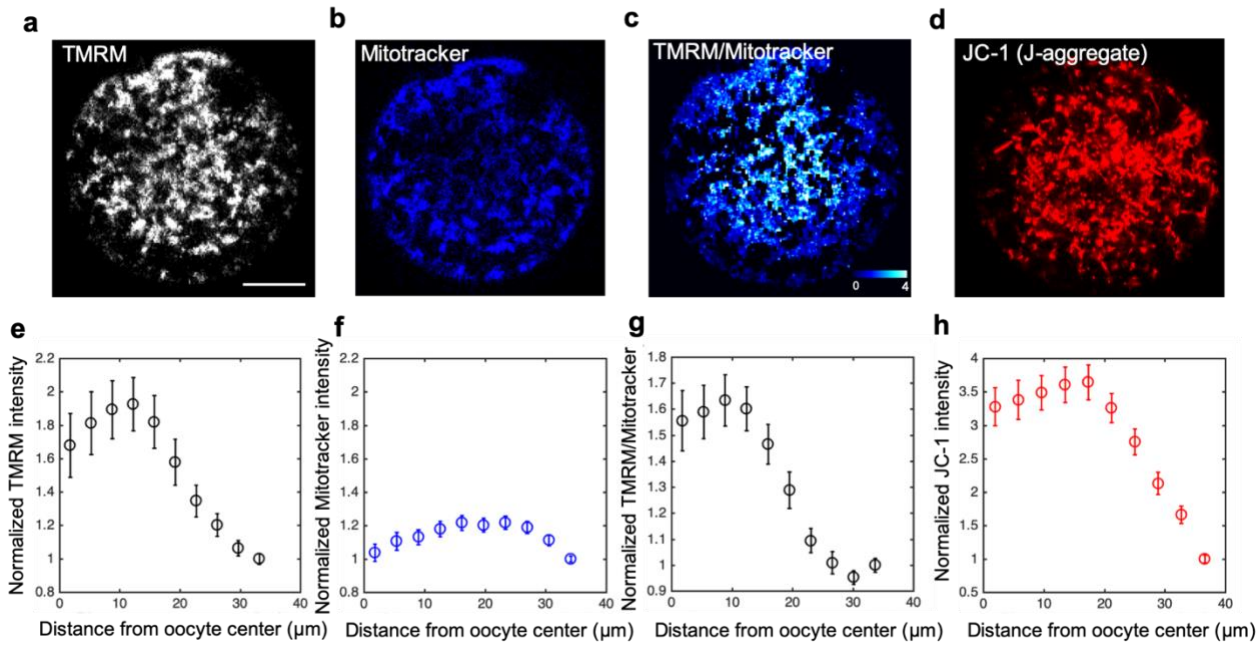


**Figure S5 | Subcellular spatial gradient of mitochondrial membrane potential. a-d,** Intensity images of TMRM, Mitotracker Red FM, TMRM/Mitotracker ratio, JC-1 (J-aggregate). **e-h**, Normalized subcellular intensity gradient of the corresponding dyes as a function of distance from the oocyte's center (n=18 for each dye).

As shown in the main text, we observed a strong spatial gradient of the intensity of TMRM in mitochondria in oocytes. TMRM is a potential-sensitive dye that preferentially accumulates in mitochondria with higher membrane potential (Figure 4 d-e in the main text). To test whether this spatial gradient is due to the subcellular variation of mitochondrial membrane potential or the variation in mitochondrial mass, we labelled mitochondria with a potential-insensitive dye Mitotracker Red FM to quantify mitochondrial mass, together with TMRM. We did not observe a strong gradient of mitotracker intensity (Figure S5 b,f) as compared to TMRM intensity (Figure S5 a,e) within the same oocyte, indicating the mitochondrial mass is uniformly distributed. We further normalized the TMRM intensity by the mitotracker intensity, and observed a strong spatial gradient of the ratio (Figure S5 c,g). These results suggest that the spatial gradient of TMRM is due to the variation of mitochondrial membrane potential, rather than the variation of mitochondrial mass. Finally, to test the robustness of the result, we used an alternative potential-sensitive dye JC-1, and observed the same spatial gradient of mitochondrial membrane potential (Figure S5 d,h). Taken together, these results show that the subcellular spatial gradient of mitochondrial membrane potential is a robust observation that does not depend on the variation of mitochondrial mass or the type of dye used.

## $\beta_{eq}$ is uniform within the oocyte

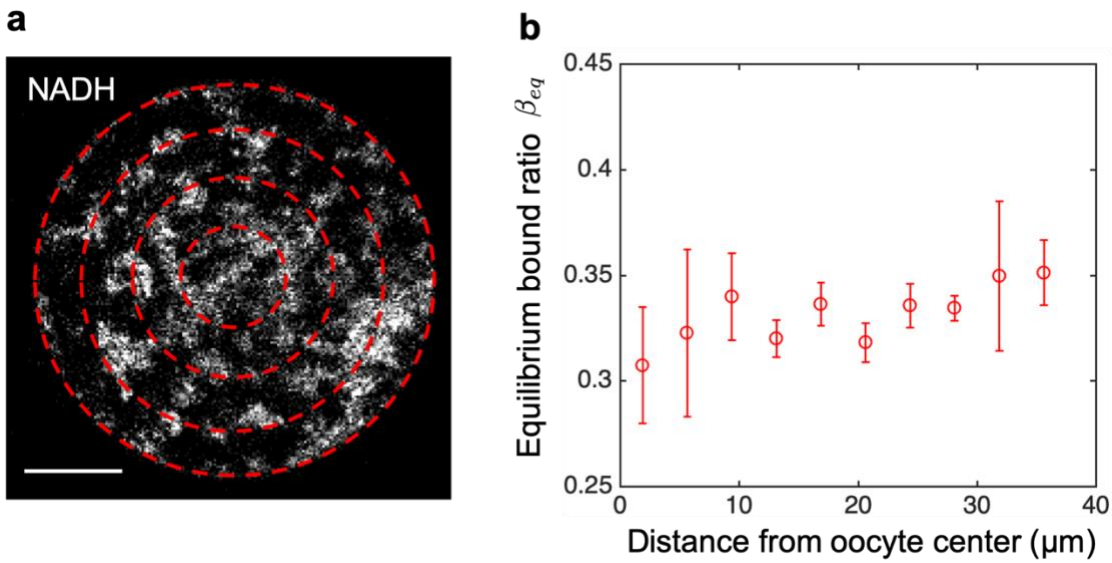


**Figure S6 | $\beta_{eq}$ is uniform within the oocyte. a,** NADH intensity image with oocyte partitioned by equal-distanced concentric rings. **b**, Equilibrium bound ratio $\beta_{eq}$ as a function of distance from the oocyte's center obtained by completely inhibiting ETC with rotenone. (n=10).

To obtain subcellular ETC flux as a function of distance to the oocyte's center using eqn. 1 in the main text, we need to know the spatial variation of $\beta_{eq}$. To obtain $\beta_{eq}$ throughout the oocyte, we inhibited the ETC completely using sodium rotenone, an inhibitor of complex I in the ETC. We then fitted the NADH decay curves from mitochondrial pixels within equal-distanced concentric rings (Figure S6a) to obtain $\beta_{eq}$ as a function of distance from the oocyte center (Figure S6b). The resulting $\beta_{eq}$ is uniform throughout the oocyte and is equal to the $\beta_{eq}$ obtained by fitting the decay curve from all mitochondrial pixels in the oocyte at the lowest oxygen level (Figure S3h). Therefore, we used the constant $\beta_{eq}$ at the lowest oxygen level to compute subcellular ETC flux (Figure 4f in the main text).

**Connecting the NADH redox model to detailed biophysical models of mitochondrial metabolism**

In this section, we show that the coarse-grained NADH redox model described above, and in Figure 2a of the main text, can be directly related to detailed biophysical models of mitochondrial metabolism, including previously published models[3-7].

In mitochondria, NADH oxidation is catalyzed by complex I of the electron transport chain, which has the overall reaction:

$$H^+ + NADH + Q \rightleftarrows NAD^+ + QH_2 + 4\Delta H^+ \ (S30),$$

where two electrons are transferred from NADH to ubiquinone Q, and 4 protons are pumped out of the mitochondrial matrix. To connect our model with detailed model of complex I, we rewrite the flux through the ETC:

$$J_{ox} = r_{ox}^{+}[NADH \cdot ox] - r_{ox}^{-}[NAD^+ \cdot ox] \ \text{(S31)},$$

Using

$$[NADH \cdot ox] = \alpha\left(\frac{\beta_{eq}^{re}}{k_{o,u}} + \frac{\beta_{eq}^{ox}}{k_{r,u}} - \frac{\beta}{k_{o,u}}\right)[NADH_f]\text{(S32)},$$
$$[NAD^+ \cdot ox] = \alpha'\left(\frac{\beta_{eq}^{'re}}{k'_{o,u}} + \frac{\beta_{eq}^{'ox}}{k'_{r,u}} - \frac{\beta'}{k'_{o,u}}\right)[NAD_f^+]\text{(S33)},$$

where

$$\alpha = \frac{k_{o,u}\,k_{r,u}}{k_{o,u}-k_{r,u}},\ \beta = \frac{[NADH_b]}{[NADH_f]},\ \ \beta_{eq}^{ox} + \beta_{eq}^{re} = \beta_{eq},\ \beta_{eq}^{ox} = \frac{k_{o,b}}{k_{o,u}},\ \ \beta_{eq}^{re} = \frac{k_{r,b}}{k_{r,u}} \ \text{(S34)}$$

$$\alpha' = \frac{k'_{o,u}\,k'_{r,u}}{k'_{o,u}-k'_{r,u}},\ \beta' = \frac{[NAD_b^+]}{[NAD_f^+]},\ \ \beta_{eq}^{'ox} + \beta_{eq}^{'re} = \beta'_{eq},\ \beta_{eq}^{'ox} = \frac{k'_{o,b}}{k'_{o,u}},\ \ \beta_{eq}^{'re} = \frac{k'_{r,b}}{k'_{r,u}} \ \text{(S35)}$$

as

$$J_{ox} = \tilde{r}_{ox}^{+}[NADH_f] - \tilde{r}_{ox}^{-}[NAD_f^+] = \tilde{r}_{ox}[NADH_f] \text{ (S36)},$$

where

$$\tilde{r}_{ox}^{+} = \alpha\left(\frac{\beta_{eq}^{re}}{k_{o,u}} + \frac{\beta_{eq}^{ox}}{k_{r,u}} - \frac{\beta}{k_{o,u}}\right) r_{ox}^{+} \text{ (S37)},$$

$$\tilde{r}_{ox}^{-} = \alpha'\left(\frac{\beta_{eq}'^{re}}{k_{o,u}'} + \frac{\beta_{eq}'^{ox}}{k_{r,u}'} - \frac{\beta'}{k_{o,u}'}\right) r_{ox}^{-} \text{ (S38)},$$

$$\tilde{r}_{ox} = \alpha(\beta - \beta_{eq}) = \left(\tilde{r}_{ox}^{+} + \tilde{r}_{ox}^{-}\frac{1+\beta}{1+\beta'}\right) - \frac{N}{[NADH_f]}\tilde{r}_{ox}^{-} (S39).$$

The last equality in Eqn.(S39) is obtained by assuming that the total concentration of NADH plus $NAD^+$ is constant:

$$N = [NADH_f] + [NAD_f^+] + [NADH_b] + [NAD_b^+] \ (S40).$$

Eqn. (S36) allows us to connect our coarse-grained model to previously published detailed models of complex I. By equating the flux through complex I, $J_{C1}$, in previous models to the flux through the ETC in our NADH redox model, $J_{ox}$, we can determine $\tilde{r}_{ox}$ (and $\tilde{r}_{ox}^{+}$ and $\tilde{r}_{ox}^{-}$) in terms of variables defined in those more detailed models. In Table S1, we summarize the relationship between the NADH redox model and several previously published models of complex I.

| Model | Flux | $\tilde{r}_{ox}^{+}$ | $\tilde{r}_{ox}^{-}$ | $\tilde{r}_{ox}$ |
|---|---|---|---|---|
| Beard (Ref[3]) | $J_{CI} = \tilde{r}_{ox}^{+}[NADH_f] - \tilde{r}_{ox}^{-}[NAD_f^+]$ | $\tilde{r}_{ox}^{+} = X_{C1}e^{\frac{\Delta\tilde{G}_{CI}}{RT}}$ | $\tilde{r}_{ox}^{-} = X_{C1}$ | $\tilde{r}_{ox} = \left(\tilde{r}_{ox}^{+} + \tilde{r}_{ox}^{-}\frac{1+\beta}{1+\beta'}\right) - \frac{N}{[NADH_f]}\tilde{r}_{ox}^{-}$ |
| Chang (Ref [4])<br>Jin (Ref[5]) | $J_{CI} = \tilde{r}_{ox}[NADH_f]$ | N/A | N/A | $\tilde{r}_{ox} = V_{max}\left(\frac{[N_T]}{[N_T]+K_{S,D}}\right)\left(\frac{[Q_T]}{[Q_T]+K_{S,A}}\right)\times \left(\frac{[Q]}{[Q]+[QH_2]K_{R,A}}\right)\left(\frac{1}{[NADH_f]+[NAD_f^+]K_{R,D}}\right)\times (1-e^{-\frac{\Delta G_{CI}}{RT}})$ |
| Hill (Ref[6]) | $J_{CI} = J_{max}(1-e^{\frac{-\Delta G_{CI}}{RT}})$ | N/A | N/A | $\tilde{r}_{ox} = J_{max}(1-e^{\frac{-\Delta G_{CI}}{RT}})/[NADH_f]$ |
| Korzeniewski (Ref[7]) | $J_{CI} = k_{CI}\Delta G_{CI}$ | N/A | N/A | $\tilde{r}_{ox} = k_{CI}\Delta G_{CI}/[NADH_f]$ |
| $\Delta G_{CI} = -[\Delta G_{0,CI} + 4\Delta G_H - RTln\left(\frac{[H^+]}{10^{-7}}\right) - RTln\left(\frac{[Q]}{[QH_2]}\right) - RTln\left(\frac{[NADH_f]}{[NAD_f^+]}\right)]$; $\Delta\tilde{G}_{CI} = \Delta G_{CI} - RTln\left(\frac{[NADH_f]}{[NAD_f^+]}\right)$; $\Delta G_{0,CI} = -69.37kJ/mol$<br>$[N_T] = [NADH_f] + [NAD_f^+]$, $[Q_T] = [Q] + [QH_2]$ | | | | |

**Table S1 | Connection of the NADH redox model to detailed models of complex I.** $\Delta G_H$ is the proton motive force. $\Delta G_{CI}$ is the free energy difference of the reaction at complex I. $\Delta G_{0,CI}$ is the standard free energy difference of the reaction at complex I.


1. Berg, S., et al., *ilastik: interactive machine learning for (bio)image analysis*, Nature Methods, 16, 1226-1232(2019)
2. Sharick, J.T., et al., *Protein-bound NAD(P)H Lifetime is Sensitive to Multiple Fates of Glucose Carbon*, Sci Rep., 2018, 8:5456
3. Beard D.A., *A biophysical model of the mitochondrial respiratory system and oxidative phosphorylation.* PLoS Comput Biol. 2005. 1(4): e36

4. Chang, I., Heiske, M., Letellier, T., Wallace, D., Baldi, P., *Modeling of Mitochondria Bioenergetics Using a Composable Chemiosmotic Energy Transduction Rate Law: Theory and Experimental Validation*, PLoS One. 2011;6(9):e14820
5. Jin, Q., Bethke, C.M., *Kinetics of Electron Transfer through the Respiratory Chain*, Biophysical Journal, Volume 83, October 2002, 1797–1808
6. Hill, T.L., *Free Energy Transduction in Biology*, (1977) Academic
7. Korzeniewski, B., Zoladz, J.A., *A model of oxidative phosphorylation in mammalian skeletal muscle*, Biophysical Chemistry, 2001, 92, 17-34